Surface Refaceting Mechanism on Cubic Ceria

Chengwu Yang,[#] Marçal Capdevila-Cortada,[#] Chunyan Dong,[#] Yan Zhou,[*] Junjun Wang, Xiaojuan Yu, Alexei Nefedov, Stefan Heißler, Núria López,[*] Wenjie Shen, Christof Wöll,[*] and Yuemin Wang[*]

ABSTRACT: Polar surfaces of solid oxides are intrinsically unstable and tend to reconstruct due to the diverging electrostatic energy and thus often exhibit unique physical and chemical properties. However, a quantitative description of the restructuring mechanism of these polar surfaces remains challenging. Here we provide an atomic-level picture of the refaceting process that governs the surface polarity compensation of cubic ceria nanoparticles based on the accurate reference data acquired from the well-defined model systems. The combined results from advanced infrared spectroscopy, atomic-resolved transmission electron microscopy, and density functional theory calculations identify a two-step scenario where an initial O-terminated (2 × 2) reconstruction is followed by a severe refaceting via massive mass transport at elevated temperatures to yield {111}-dominated nanopyramids. This significant surface restructuring promotes the redox properties of ceria nanocubes, which account for the enhanced catalytic activity for CO oxidation.

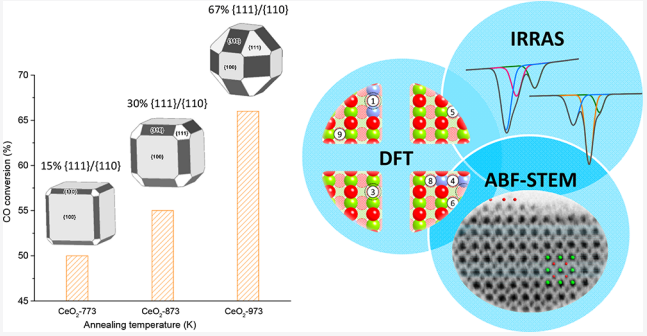

Ceria is one of the most important metal oxides in heterogeneous catalysts and is an essential component that largely relies on its unique redox properties that primarily originate from the quick and reversible redox cycle between Ce^{4+} and Ce^{3+} in the fluorite lattice under alternatively oxidative and reductive atmospheres.[1,2] Experimental and theoretical studies have verified that this redox character is intimately linked to the shape at the nanometer level, which commonly presents as octahedra, rods, and cubes.[3−5] In particular, cube-shaped CeO_2 nanoparticles exposing polar {100} facets feature unique physical and chemical properties.[6−12] However, they could considerably alter the reactivity at high temperatures or under reactive gases due to the surface restructuring driven by the polar instability.[13−15] It is known that bulk-truncated polar oxide surfaces are intrinsically unstable due to the presence of a macroscopic dipole moment along the surface normal.[16] The stabilization mechanism involves complex atomic rearrangements of the outermost layer and the sublayers for lowering the overall surface energy and significant charge redistributions for eliminating the electrostatic imbalance (i.e., polarity compensation).[17−22]

Currently, two rather different reconstruction models for the ceria (100) surface are being discussed.[23−28] One is O-terminated (O-t), where electrostatic stability is recovered by removing 50% of surface oxygen atoms, yielding an O-t (2 × 2) structure. The other corresponds to a Ce termination and is obtained by adding one cerium and two oxygen ions at the positions of a (2 × 2) lattice, forming CeO_4 square pyramids. According to density functional theory (DFT) simulations, the energies of these two polarity-compensated surface structures are very close.[27] It remains challenging to experimentally and unambiguously identify the detailed mechanism of surface restructuring on ceria nanocubes. A lack of reliable experimental input hampers the derivation of structure−activity relationships.

Herein we report a comprehensive study on polar ceria (100) surfaces of both well-defined single crystals and powdered nanocubes using a multitechnique approach. The atomic structural evolution of the polar (100) surface was investigated by polarization-resolved IR reflection absorption spectroscopy (IRRAS) and atomic-resolved high-resolution (scanning) transmission electron microscopy (HRTEM/STEM). The experimental results were rationalized using DFT calculations.

We initially synthesized well-crystallized CeO_2 cubes of ∼20 nm, which predominantly exposed the polar {100} facets.[29] As shown in Figure 1a and Figures S1 and S2, SEM/HRTEM images verified the nearly perfect cube-like shape. The atomic-resolved STEM image, viewed along the [001] direction, affirmed that the cube mainly exposed {100} facets on the flat surfaces, with minor {110} facets at the edges and {111} facets

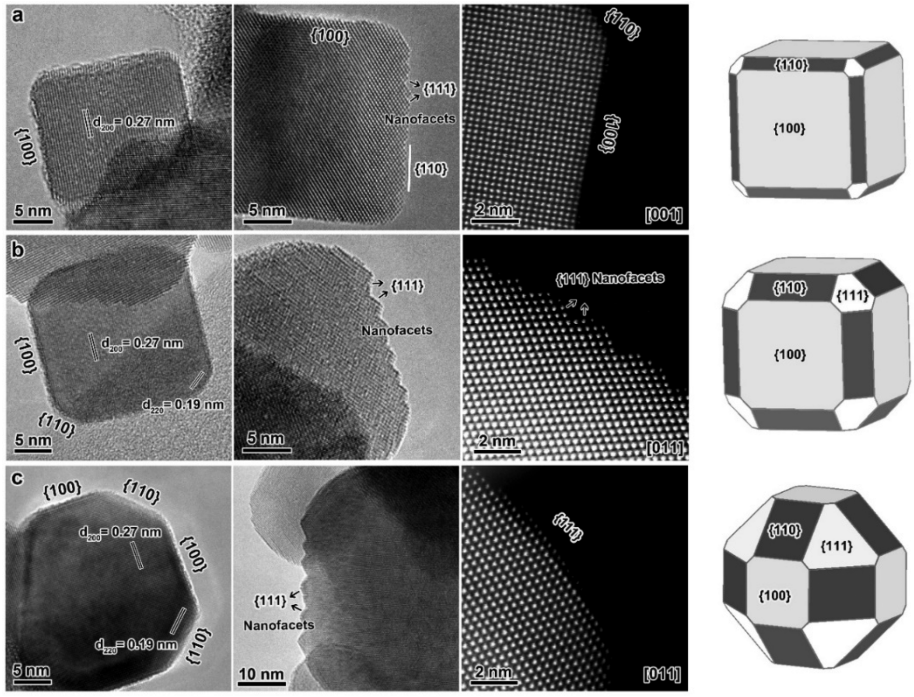

Figure 1. Structural evolution of ceria nanocubes. HRTEM/STEM images and morphological model of ceria nanocubes obtained after annealing in air at (a) 773, (b) 873, and (c) 973 K.

at the corners. The STEM image, viewed along the [011] zone axis, further identified that the {110} planes at the edges consisted of sawtooth-like {111} facets. Overall, the square, flat surfaces of the nanocubes are enclosed by the {100} facets, whereas the truncated edges and corners are terminated by the {110} and {111} planes.[14,30−33] Furthermore, the annular bright field (ABF) images along both the [001] and [011] directions (Figure S2e,f) provide evidence of the O-terminated {100} surfaces.

To examine the surface structural evolution, the ceria nanocubes were further calcined at 873−973 K (Figure 1 and Figure S3). Upon further thermal treatment, the mean size of the cubic ceria did not change obviously, slightly ranging from 22 to 25 nm, but the surface restructuring remarkably occurred. A detailed analysis of the representative HRTEM/STEM data revealed that the planar {100} facets substantially reduced with increasing temperature, whereas the fraction of the {111} and {110} facets enhanced significantly. The polarity compensation at the polar {100} surfaces induced the development of extended flat {111} facets (corner-truncated) and {110} planes (edge-truncated). The latter was fully {111}-faceted, exposing a characteristic sawtooth-like structure.[34] Accordingly, all nanofaceted planes exposed a {111} orientation. Along with the massive morphological modification, the population of the {100} surfaces gradually decreased from 85% at 773 K to 33% at 973 K, whereas the {111} facets, that is, (110) + (111), became the most abundant ones at 973 K (Table S1). These observations reveal that after heating to elevated temperatures, the polar {100} planes of ceria nanocubes undergo massive restructuring, forming more stable {111} facets at the edges and corners.

The impact of this surface refaceting on the catalytic property of ceria nanocubes was evaluated by CO oxidation at 673 K. In brief, the conversion of CO gradually increased with the fraction of the {111} facets (including the {111}-faceted {110} planes; Figure 2 and Figure S4) rather than the surface area or the particle size, as generally viewed. This result clearly

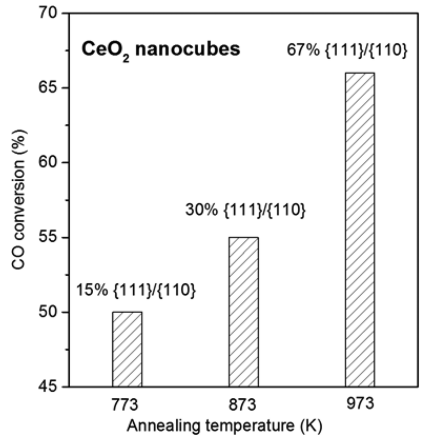

Figure 2. Evaluation of the catalytic property. CO oxidation over the CeO_2 nanocubes calcined at different temperatures (773−973 K) in air. Reaction conditions: 1 vol % CO/20 vol % O_2/He, 673 K, 37 500 mL g_{cat}^{-1} h^{-1}.

demonstrates that the surface refaceting on cubic ceria, by exposing more {111}/{110} planes at the edges and corners, substantially enhanced the catalytic activity. This is likely related to the improvement of the redox properties of ceria by considering the fact that CO oxidation on ceria at 673 K follows the Mars−van Krevelen mechanism, involving the Ce^{4+}/Ce^{3+} redox couple and oxygen vacancy formation.[35] Therefore, the higher activity observed on the high-temperature-treated samples is associated with the increased number of active sites generated by the surface refaceting, as will be discussed later.

To elucidate the mechanism of the surface refaceting on ceria nanocubes, we adapted IRRAS using CO as a probe molecule and DFT calculations to comparatively examine the situations on both the well-defined single crystals and the practical powders. Initially, a surface-science approach was used to determine the surface structures involved in the O- and Ce-terminated models. The vibrational frequency of adsorbed CO has been proven to be very sensitive to adsorption sites exposed by metal oxide surfaces.[36−38] Indeed, our DFT confirmed the pronounced differences in the CO stretch frequencies in the two models. In the case of the O-terminated (2 × 2) structure, all CO vibrational bands for oxidized and defective CeO_2(100) surfaces are blue-shifted compared with the gas-phase value (Figure 3, Table 1). In contrast, for the CeO_4-terminated (2 × 2) structure (Figure S5), only for the ideal surface does the ν(C−O) vibration exhibit a slight blue shift, whereas all defect-related CO species show red shifts (Table S2).

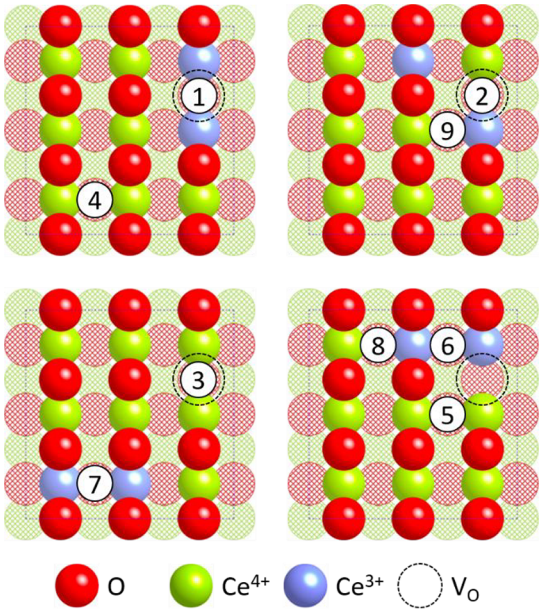

Figure 3. Identification of CO absorption sites on ceria (100). Different adsorption sites of CO (marked by numbers) on (2 × 2) O-t ceria (100) obtained from DFT calculations.

Table 1. Stretch-Vibration Frequencies (ν_{calc}) and Binding Energies (E_b) Obtained from DFT (PBE+U) Calculations for CO Adsorbed at Different Sites on (2 × 2) O-t Ceria (100)[a]

site no.	adsorption site	ν_{calc} (cm^{-1}) (E_b/eV)	ν_{exp} (cm^{-1})
1	Ce^{3+}−Ce^{3+} on V_O	2171.3 (−0.47)	2168
2	Ce^{3+}−Ce^{4+} on V_O	2170.9 (−0.41)	
3	Ce^{4+}−Ce^{4+} on V_O	2175.7 (−0.15)[b]	2176
4	Ce^{4+}−Ce^{4+} far from V_O	2144.3 (−0.52)	2147
5	Ce^{4+}−Ce^{4+} next to V_O	2146.2 (−0.51)	
6	Ce^{3+}−Ce^{3+} next to V_O	2154.8 (−0.46)	
7	Ce^{3+}−Ce^{3+} far from V_O	2151.0 (−0.12)[b]	
8	Ce^{3+}−Ce^{4+} far from V_O	2150.7 (−0.45)	
9	Ce^{3+}−Ce^{4+} next to V_O	2149.8 (−0.49)	

[a]Experimental data (ν_{exp}) are also provided. [b]Weaker binding energy for site nos. 3 and 7 is due to the fact that all binding energies have been obtained taking the most stable surface as the reference, which has the two Ce^{3+} centers close to the V_O site, whereas site nos. 3 and 7 require both Ce^{3+} centers to be away from V_O. When accounting for this slightly unfavorable configuration, their binding energies fall within the expected range (−0.49 and −0.47 eV, respectively).

Well-ordered ceria (100) single-crystal surfaces were prepared by gently annealing at 800 K in oxygen and subsequently exposing to O_2 at 75 K, followed by heating to room temperature. Low-energy electron diffraction (LEED) results exhibit a clear (2 × 2) pattern (Figure 4b); the lattice

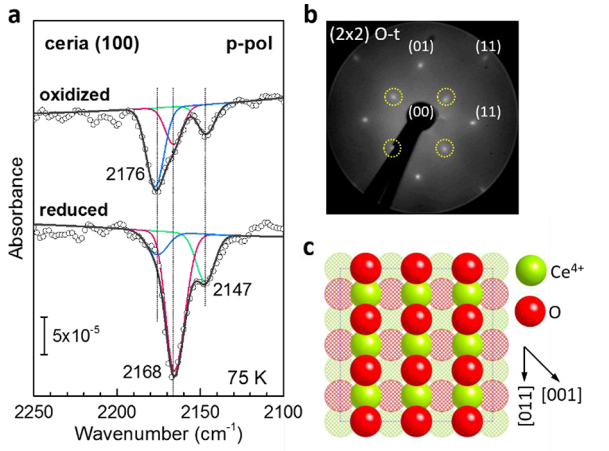

Figure 4. O-terminated (2 × 2) CeO_2(100) characterized by IRRAS and LEED. (a) p-polarized IRRA spectra of CO adsorption at 75 K on oxidized and reduced ceria (100) single crystals. (b) LEED pattern of O-t (2 × 2) ceria (100) surface with electron-beam energy of 90 eV. The well-defined fractional order reflections are indicated by yellow dashed circles. (c) Surface structure of the O-t (2 × 2) ceria (100) surface.

constant α_{CeO_2} was determined to be ∼0.39 nm.[24,39] From grazing-emission X-ray photoelectron spectroscopy (XPS) data (Figure S6), we estimated a surface concentration of ∼15% Ce^{3+}, revealing that even after careful oxidation treatments, the concentration of oxygen vacancies (V_O) is still substantial. This observation is in line with the low activation energies needed to create V_O on this highly reducible surface.[11]

The polarization-resolved infrared reflection absorption spectroscopy (IRRAS) data for CO adsorbed on the oxidized surface (Figure 4a) reveals an intense band at 2176 cm^{-1} with a shoulder at 2168 cm^{-1} and a second weaker peak at 2147 cm^{-1}. Upon further reducing the surface by annealing to 800 K under ultrahigh vacuum (UHV) conditions, we observe a shift of the main band from 2176 to 2168 cm^{-1}, whereas the frequency of the low-lying band remains unchanged at 2147 cm^{-1}. Here an unambiguous assignment of the IR bands becomes possible by considering the results of DFT calculations (Table 1). In these simulations, in addition to the stoichiometric (2 × 2) surface, a number of different defect structures were considered (Figure 3). The binding energies for all adsorption sites are rather similar, in the range of −0.41 to −0.52 eV. The DFT results for the CeO_4 termination (Figure S5, Table S2), with binding energies ranging from −0.30 to −0.44 eV, show pronounced red shifts for all defect related CO species, which are clearly not observed in IRRAS.

For the O-terminated (2 × 2) CeO_2(100) surface, Table 1 reveals a much better agreement between experimental and computed frequencies. All CO vibrations, for the stoichiometric as well as for the reduced surface, are blue-shifted. The

IR signal at 2147 cm^{-1} is ascribed to CO adsorbed to Ce^{4+} sites (Figure 3, nos. 4 and 5), located either at ideal patches of the surface or at some distance from O-vacancies. The 2168 cm^{-1} band is assigned to CO bound at the Ce^{3+} sites next to O-vacancies within reduced patches (Figure 3, nos. 1 and 2), whereas the 2176 cm^{-1} vibration is attributed to CO adsorbed at low-coordinated (five-fold) Ce^{4+} sites (no. 3). The minority species, located at nonvacancy Ce^{3+} sites of the reduced O-t (2 × 2) surface (nos. 6–9, 2155–2150 cm^{-1} in Table 1), are not resolved from the main IR band at 2168 cm^{-1} due to their low concentration, also considering that a portion of Ce^{3+} centers are localized at subsurface or bulk positions. On the basis of the combined IRRAS and DFT results, we conclude that the relevant surface structure for polarity-compensated CeO_2(100) follows an O-terminated (2 × 2) reconstruction.

When subjecting the CeO_2 single crystals to repeated annealing cycles at higher temperatures (850 and 900 K), which resemble those used in technical catalytic applications of ceria, the pronounced changes in IRRAS (Figure 5a) reveal a

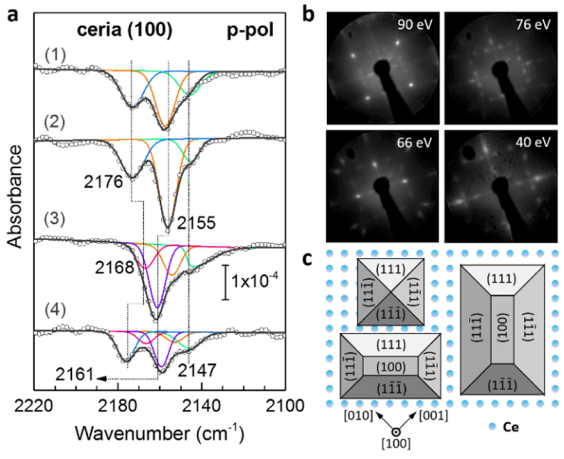

Figure 5. {111}-Faceted ceria (100) characterized by IRRAS and LEED. (a) p-polarized IRRAS data of CO adsorption on ceria (100) surfaces at 75 K after (1) Ar^+ sputtering and annealing in an O_2 atmosphere at 850 K, (2) Ar^+ sputtering and annealing in O_2 at 900 K, (3) annealing at 900 K under UHV conditions, and (4) low-temperature O_2 treatment. (b) Motion of facet spots in LEED patterns of {111}-faceted ceria (100) as a function of electron-beam energy. (c) Schematic representation of the {111}-faceted ceria (100).

transformation of the surface to a rather different state, indicating the presence of one more stable polarity compensation. First, the p-polarized IRRAS data show a new band at 2155 cm^{-1} (Figure 5a, curve 1), which becomes the predominant one along with further annealing to 900 K in O_2 (curve 2). A subsequent heating to 900 K in the absence of O_2 leads to the formation of a highly reduced surface, as confirmed by the shift of the 2176 cm^{-1} band to 2168 cm^{-1} characteristic for Ce^{3+} sites at O vacancies on CeO_2(100). Simultaneously, the main IR band shifts to 2161 cm^{-1} (curve 3).

The appearance of these new features suggests a complex nature of the surface restructuring, yielding terminations different from (100). Indeed, the frequencies of the new bands resemble those reported for the CeO_2(111) surface.[40] Our DFT calculations allowed for an unambiguous assignment of the vibrations at 2155 and 2161 cm^{-1} to CO molecules adsorbed on stoichiometric and defect-related surface patches exposing a (111) termination (Table S3). Again, there is an excellent agreement between experiment and theory. This assignment is further supported by the observation that the defect-related signal at 2161 cm^{-1} remained unchanged after exposure to O_2 (Figure 5a, curve 4), which is a fingerprint for the presence of (111) facets where oxygen vacancies are unstable in the top plane but are located in sublayers.[41] In contrast, the reduced (100)-related CO band at 2168 cm^{-1} shifts back to 2176 cm^{-1} upon oxidation (curve 4), revealing the occurrence of O_2 activation on the nonfaceted (100) surface.

Additional evidence of the massive restructuring is provided by considering the polarization dependence of IRRAS. When applying IRRAS to dielectric substrates, the intensity and sign of vibrational bands depend on the interaction of the transition dipole moment (TDM) with p-polarized (normal, $E_{p,n}$; tangential, $E_{p,t}$) and s-polarized (E_s) components of the incident light.[36] For the flat (100) surface, the negative sign in the p-polarized spectra reveals that the CO vibration is primarily excited via coupling to $E_{p,n}$, which is fully consistent with these CO species adopting a nearly upright geometry predicted by our DFT calculations. For this orientation, the CO vibrations are invisible in the s-polarized data (Figure S7) because the TDM is orthogonal to the E_s vector. However, after the temperature-induced restructuring, the s-polarized spectra clearly show peaks at 2154 and 2160 cm^{-1} (Figure S7) assigned to CO adsorbed on (111) surfaces (Table S3). These results reveal the presence of {111} nanofacets, where the CO-TDM is tilted by ~35° with respect to the (100) plane (Figure 5C), thus making CO vibrations in s-polarized light visible.

Moreover, LEED patterns indicate massive morphological changes resulting from the heating cycles. As shown in Figure 5b and Figure S8, the (2 × 2)-pattern for the nonfaceted surface has vanished, and, instead, a large number of diffraction spots attributed to {111} facets appear. The spot positions vary strongly depending on the electron energy, an observation indicating the formation of {111}-faceted nanopyramids (Figure 5c).[42−44]

Overall, these experimental and theoretical results consistently demonstrate that the polarity compensation of CeO_2(100) is initiated by the O-terminated (2 × 2) reconstruction. Upon further heating to elevated temperatures (>850 K), a second substantial restructuring occurs, where the original polar instability is removed through an extensive {111} nanofaceting. The transition to this second step is kinetically hindered because of the large mass transport required.

To verify this restructuring mechanism for the practical nanocubes, we compared Fourier transform infrared (FTIR) spectra recorded for CO adsorbed on ceria nanocubes with the IRRAS data of the well-defined single crystals. The frequencies of CO molecules adsorbed on cubic ceria nanoparticles, after reduction (Figure 6a) as well as after oxidation (Figure 6b), are very similar to those observed on the model system. In brief, after a mild heating of the nanocubes at 750 K, three IR bands are observed at 2174, 2166, and 2149 cm^{-1}, which can be assigned by using the results for the O-terminated (2 × 2) ceria (100) surface. (For details, see Table 1.) This finding agrees with HRTEM/STEM data (Figure 1a–c, Figure S2), which show that these nanoparticles (pretreated at 773 K) are almost perfect {100}-truncated cubes, with a very small portion of {110} facets at the edges and {111} facets at the corners. Note that the surface O atoms are rather mobile at room temperature.[27,45,46]

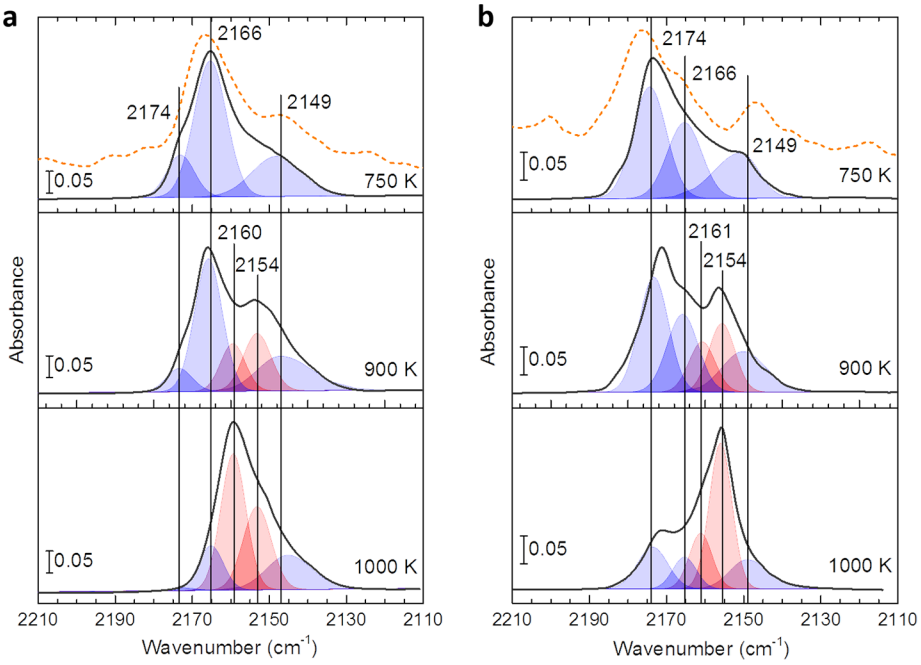

Figure 6. Structural evolution of ceria nanocubes characterized by CO surface-ligand infrared spectroscopy (CO-SLIR). (a) Deconvoluted FTIR spectra of CO adsorption at 65 K on ceria nanocubes pretreated by heating to the indicated temperatures (reduced) and (b) then exposing to O_2 at low temperatures followed by warming to room temperature (oxidized). For comparison, the corresponding IRRAS data (Figure 4a) of CO adsorption on O-t (2 × 2) CeO_2(100) single-crystal surfaces are shown as dashed curves with a reversed sign.

When subjected to annealing at higher temperatures (900 and 1000 K), the behavior of the nanocubes under reductive and oxidative conditions is quite similar to that of the model systems, as confirmed by the corresponding IR spectra (Figure 6). The appearance and growth of two typical CO bands at 2154 and 2160 cm^{-1}, originating from {111} facets, reveal the pronounced restructuring, in excellent agreement with the results for monocrystalline surfaces. These IR results solidly support the surface refaceting presented in the HRTEM/STEM images of ceria nanocubes (Figure 1). A quantitative analysis of the IR data in Figure 6 shows that the relative intensity of the {111}-related CO bands was ca. 30% at 900 K and 65% at 1000 K, in line with the structural evolution visualized by HRTEM/STEM. Overall, the combined results reveal that the restructuring of ceria nanocubes primarily results from the inherent polarity instability and subsequently yields a strongly {111}-faceted surface.

Importantly, the surface refaceting is accompanied by a significant increase in the subsurface O vacancies on {111} facets, as confirmed by the characteristic CO band at 2160 cm^{-1} (Figure 6, Table S3). This conclusion is supported by the direct observation of Ce^{3+}-related electronic excitations ($2F_{5/2} \rightarrow 2F_{7/2}$) at 2120 cm^{-1} (Figure S9).[47] Furthermore, the content of corner and edge atoms with reduced coordination numbers greatly increases along with the massive restructuring, as shown in HRTEM/STEM (Figure 1). We propose that the improved redox properties via creating more V_O defects dominantly contribute to the enhanced catalytic activity for CO oxidation, likely by trapping O_2.

In summary, we found that the catalytic activity of ceria nanocubes for CO oxidation varies strongly along with the complex structural evolution driven by the inherent polar instability of {100} surfaces. The combined results from advanced IR spectroscopy, HRTEM/STEM, and DFT calculations convincingly evidenced that the restructuring on the polar ceria (100) surface initially leads to an O-t (2 × 2) configuration. When the material is subjected to temperatures above 800 K, which is typical for catalytic processes, further massive restructuring occurs, yielding {111}-faceted surfaces. This second step requires massive mass transport and is thus kinetically hindered. The substantial surface refaceting improves the redox properties of cubic ceria by creating more O vacancies and low-coordinated defect sites, which account for the enhanced catalytic activity for CO oxidation. This two-step scenario could also be viewed as a polarity compensation mechanism for other ionic oxides.

■ ASSOCIATED CONTENT

Supporting Information

The Supporting Information is available free of charge at .

Experimental and computational details; additional results obtained from HRTEM/STEM/SEM, catalytic evaluation, DFT calculations, XPS, LEED, as well as IR investigations (PDF)

■ AUTHOR INFORMATION

Corresponding Authors

Yan Zhou − *State Key Laboratory of Catalysis, Dalian Institute of Chemical Physics, Chinese Academy of Sciences, Dalian 116023, China;* orcid.org/0000-0002-9847-0806; Email: zhouyan@dicp.ac.cn

Núria López − *Institute of Chemical Research of Catalonia (ICIQ), The Barcelona Institute of Science and Technology, 43007 Tarragona, Spain;* orcid.org/0000-0001-9150-5941; Email: nlopez@iciq.es

Christof Wöll − *Institute of Functional Interfaces (IFG), Karlsruhe Institute of Technology (KIT), 76344 Eggenstein-*

Leopoldshafen, Germany; orcid.org/0000-0003-1078-3304; Email: christof.woell@kit.edu

Yuemin Wang − *Institute of Functional Interfaces (IFG), Karlsruhe Institute of Technology (KIT), 76344 Eggenstein-Leopoldshafen, Germany;* orcid.org/0000-0002-9963-5473; Email: yuemin.wang@kit.edu

Authors

Chengwu Yang − *Beijing Key Laboratory of Bio-inspired Energy Materials and Devices, School of Space and Environment, Beihang University, Beijing 102206, China; Institute of Functional Interfaces (IFG), Karlsruhe Institute of Technology (KIT), 76344 Eggenstein-Leopoldshafen, Germany*

Marçal Capdevila-Cortada − *Institute of Chemical Research of Catalonia (ICIQ), The Barcelona Institute of Science and Technology, 43007 Tarragona, Spain;* orcid.org/0000-0003-4391-6580

Chunyan Dong − *State Key Laboratory of Catalysis, Dalian Institute of Chemical Physics, Chinese Academy of Sciences, Dalian 116023, China; University of Chinese Academy of Sciences, Beijing 100049, China*

Junjun Wang − *Institute of Functional Interfaces (IFG), Karlsruhe Institute of Technology (KIT), 76344 Eggenstein-Leopoldshafen, Germany*

Xiaojuan Yu − *Institute of Functional Interfaces (IFG), Karlsruhe Institute of Technology (KIT), 76344 Eggenstein-Leopoldshafen, Germany*

Alexei Nefedov − *Institute of Functional Interfaces (IFG), Karlsruhe Institute of Technology (KIT), 76344 Eggenstein-Leopoldshafen, Germany;* orcid.org/0000-0003-2771-6386

Stefan Heißler − *Institute of Functional Interfaces (IFG), Karlsruhe Institute of Technology (KIT), 76344 Eggenstein-Leopoldshafen, Germany*

Wenjie Shen − *State Key Laboratory of Catalysis, Dalian Institute of Chemical Physics, Chinese Academy of Sciences, Dalian 116023, China*

Complete contact information is available at:

Author Contributions

#C.Y., M.C.-C., and C.D. contributed equally.

Notes

The authors declare no competing financial interest.

■ ACKNOWLEDGMENTS

This work was supported by the German DFG (WA 2535/2-1), the German HGF "Science and Technology of Nanosystems" Programme (432202), and the National Natural Science Foundation of China (21761132031, U1832174, 21902005). M.C.-C. and N.L. thank the BSC-RES for providing generous computational resources.

■ REFERENCES

(1) Aneggi, E.; Boaro, M.; Leitenburg, C. d.; Dolcetti, G.; Trovarelli, A. Insights into the Redox Properties of Ceria-based Oxides and their Implications in Catalysis. *J. Alloys Compd.* **2006**, *408*−*412*, 1096−1102.

(2) Montini, T.; Melchionna, M.; Monai, M.; Fornasiero, P. Fundamentals and Catalytic Applications of CeO_2-Based Materials. *Chem. Rev.* **2016**, *116*, 5987−6041.

(3) Trovarelli, A.; Llorca, J. Ceria Catalysts at Nanoscale: How Do Crystal Shapes Shape Catalysis? *ACS Catal.* **2017**, *7*, 4716−4735.

(4) Li, Y.; Shen, W. Morphology-dependent Nanocatalysts: Rod-shaped Oxides. *Chem. Soc. Rev.* **2014**, *43*, 1543−1574.

(5) Huang, W.; Gao, Y. Morphology-dependent Surface Chemistry and Catalysis of CeO_2 nanocrystals. *Catal. Sci. Technol.* **2014**, *4*, 3772−3784.

(6) Mai, H.-X.; Sun, L.-D.; Zhang, Y.-W.; Si, R.; Feng, W.; Zhang, H.-P.; Liu, H.-C.; Yan, C.-H. Shape-Selective Synthesis and Oxygen Storage Behavior of Ceria Nanopolyhedra, Nanorods, and Nanocubes. *J. Phys. Chem. B* **2005**, *109*, 24380−24385.

(7) Zhou, K.; Wang, X.; Sun, X.; Peng, Q.; Li, Y. Enhanced Catalytic Activity of Ceria Nanorods from Well-defined Reactive Crystal Planes. *J. Catal.* **2005**, *229*, 206−212.

(8) Tana; Zhang, M.; Li, J.; Li, H.; Li, Y.; Shen, W. Morphology-dependent Redox and Catalytic Properties of CeO_2 Nanostructures: Nanowires, Nanorods and Nanoparticles. *Catal. Today* **2009**, *148*, 179−183.

(9) Ma, Y.; Gao, W.; Zhang, Z.; Zhang, S.; Tian, Z.; Liu, Y.; Ho, J. C.; Qu, Y. Regulating the Surface of Nanoceria and its Applications in Heterogeneous Catalysis. *Surf. Sci. Rep.* **2018**, *73*, 1−36.

(10) Baudin, M.; Wójcik, M.; Hermansson, K. Dynamics, Structure and Energetics of the (111), (011) and (001) Surfaces of Ceria. *Surf. Sci.* **2000**, *468*, 51−61.

(11) Paier, J.; Penschke, C.; Sauer, J. Oxygen Defects and Surface Chemistry of Ceria: Quantum Chemical Studies Compared to Experiment. *Chem. Rev.* **2013**, *113*, 3949−3985.

(12) Nolan, M.; Grigoleit, S.; Sayle, D. C.; Parker, S. C.; Watson, G. W. Density Functional Theory Studies of the Structure and Electronic Structure of Pure and Defective Low Index Surfaces of Ceria. *Surf. Sci.* **2005**, *576*, 217−229.

(13) Wu, Z.; Li, M.; Overbury, S. H. On the Structure Dependence of CO Oxidation over CeO_2 Nanocrystals with Well-defined Surface Planes. *J. Catal.* **2012**, *285*, 61−73.

(14) Aneggi, E.; Wiater, D.; de Leitenburg, C.; Llorca, J.; Trovarelli, A. Shape-Dependent Activity of Ceria in Soot Combustion. *ACS Catal.* **2014**, *4*, 172−181.

(15) Vile, G.; Colussi, S.; Krumeich, F.; Trovarelli, A.; Perez-Ramirez, J. Opposite Face Sensitivity of CeO_2 in Hydrogenation and Oxidation Catalysis. *Angew. Chem., Int. Ed.* **2014**, *53*, 12069−12072.

(16) Tasker, P. W. The Stability of Ionic Crystal Surfaces. *J. Phys. C: Solid State Phys.* **1979**, *12*, 4977−4984.

(17) Wöll, C. The Chemistry and Physics of Zinc Oxide Surfaces. *Prog. Surf. Sci.* **2007**, *82*, 55−120.

(18) Wander, A.; Schedin, F.; Steadman, P.; Norris, A.; McGrath, R.; Turner, T. S.; Thornton, G.; Harrison, N. M. Stability of Polar Oxide Surfaces. *Phys. Rev. Lett.* **2001**, *86*, 3811−3814.

(19) Enterkin, J. A.; Subramanian, A. K.; Russell, B. C.; Castell, M. R.; Poeppelmeier, K. R.; Marks, L. D. A Homologous Series of Structures on the Surface of $SrTiO_3$(110). *Nat. Mater.* **2010**, *9*, 245−248.

(20) Marks, L. D.; Chiaramonti, A. N.; Rahman, S. U.; Castell, M. R. Transition from Order to Configurational Disorder for Surface Reconstructions on $SrTiO_3$(111). *Phys. Rev. Lett.* **2015**, *114*, 226101.

(21) Noguera, C.; Goniakowski, J. Polarity in Oxide Nano-objects. *Chem. Rev.* **2013**, *113*, 4073−4105.

(22) Setvin, M.; Reticcioli, M.; Poelzleitner, F.; Hulva, J.; Schmid, M.; Boatner, L. A.; Franchini, C.; Diebold, U. Polarity Compensation Mechanisms on the Perovskite Surface $KTaO_3$(001). *Science* **2018**, *359*, 572−575.

(23) Herman, G. S. Surface Structure Determination of CeO_2(001) by Angle-resolved Mass Spectroscopy of Recoiled Ions. *Phys. Rev. B: Condens. Matter Mater. Phys.* **1999**, *59*, 14899−14902.

(24) Nörenberg, H.; Harding, J. H. The Surface Structure of CeO_2(001) Single Crystals Studied by Elevated Temperature STM. *Surf. Sci.* **2001**, *477*, 17−24.

(25) Skorodumova, N. V.; Baudin, M.; Hermansson, K. Surface Properties of CeO_2 from First Principles. *Phys. Rev. B: Condens. Matter Mater. Phys.* **2004**, *69*, 075401.

(26) Pan, Y.; Nilius, N.; Stiehler, C.; Freund, H.-J.; Goniakowski, J.; Noguera, C. Ceria Nanocrystals Exposing Wide (100) Facets:

Structure and Polarity Compensation. *Adv. Mater. Interfaces* **2014**, *1*, 1400404.
(27) Capdevila-Cortada, M.; López, N. Entropic Contributions Enhance Polarity Compensation for CeO_2(100) surfaces. *Nat. Mater.* **2017**, *16*, 328−334.
(28) Chen, J.; Wu, X.-P.; Hope, M. A.; Qian, K.; Halat, D. M.; Liu, T.; Li, Y.; Shen, L.; Ke, X.; Wen, Y.; Du, J.-H.; Magusin, P. C. M. M.; Paul, S.; Ding, W.; Gong, X.-Q.; Grey, C. P.; Peng, L. Polar Surface Structure of Oxide Nanocrystals Revealed with Solid-state NMR Spectroscopy. *Nat. Commun.* **2019**, *10*, 5420.
(29) Dong, C. Y.; Zhou, Y.; Ta, N.; Shen, W. Formation Mechanism and Size Control of Ceria Nanocubes. *CrystEngComm* **2020**, *22*, 3033−3041.
(30) Bhatta, U. M.; Ross, I. M.; Sayle, T. X. T.; Sayle, D. C.; Parker, S. C.; Reid, D.; Seal, S.; Kumar, A.; Möbus, G. Cationic Surface Reconstructions on Cerium Oxide Nanocrystals: An Aberration-Corrected HRTEM Study. *ACS Nano* **2012**, *6*, 421−430.
(31) Lin, Y.; Wu, Z.; Wen, J.; Poeppelmeier, K. R.; Marks, L. D. Imaging the Atomic Surface Structures of CeO_2 Nanoparticles. *Nano Lett.* **2014**, *14*, 191−196.
(32) Tinoco, M.; Fernandez-Garcia, S.; Lopez-Haro, M.; Hungria, A. B.; Chen, X.; Blanco, G.; Perez-Omil, J. A.; Collins, S. E.; Okuno, H.; Calvino, J. J. Critical Influence of Nanofaceting on the Preparation and Performance of Supported Gold Catalysts. *ACS Catal.* **2015**, *5*, 3504−3513.
(33) Hao, X.; Chen, C.; Saito, M.; Yin, D.; Inoue, K.; Takami, S.; Adschiri, T.; Ikuhara, Y. Direct Imaging for Single Molecular Chain of Surfactant on CeO_2 Nanocrystals. *Small* **2018**, *14*, 1801093.
(34) Yang, C.; Yu, X.; Heißler, S.; Nefedov, A.; Colussi, S.; Llorca, J.; Trovarelli, A.; Wang, Y.; Wöll, C. Surface Faceting and Reconstruction of Ceria Nanoparticles. *Angew. Chem., Int. Ed.* **2017**, *56*, 375−379.
(35) Trovarelli, A. Catalytic Properties of Ceria and CeO_2-Containing Materials. *Catal. Rev.: Sci. Eng.* **1996**, *38*, 439−520.
(36) Wang, Y.; Wöll, C. IR Spectroscopic Investigations of Chemical and Photochemical Reactions on Metal Oxides: Bridging the Materials Gap. *Chem. Soc. Rev.* **2017**, *46*, 1875−1932.
(37) Chen, A.; Yu, X.; Zhou, Y.; Miao, S.; Li, Y.; Kuld, S.; Sehested, J.; Liu, J.; Aoki, T.; Hong, S.; Camellone, M. F.; Fabris, S.; Ning, J.; Jin, C.; Yang, C.; Nefedov, A.; Wöll, C.; Wang, Y.; Shen, W. Structure of the Catalytically Active Copper−ceria Interfacial Perimeter. *Nat. Catal.* **2019**, *2*, 334−341.
(38) Wöll, C. Structure and Chemical Properties of Oxide Nanoparticles Determined by Surface-Ligand IR Spectroscopy. *ACS Catal.* **2020**, *10*, 168−176.
(39) Kim, Y. J.; Gao, Y.; Herman, G. S.; Thevuthasan, S.; Jiang, W.; McCready, D. E.; Chambers, S. A. Growth and Structure of Epitaxial CeO_2 by Oxygen-plasma-assisted Molecular Beam Epitaxy. *J. Vac. Sci. Technol., A* **1999**, *17*, 926−935.
(40) Yang, C.; Yin, L.-L.; Bebensee, F.; Buchholz, M.; Sezen, H.; Heissler, S.; Chen, J.; Nefedov, A.; Idriss, H.; Gong, X.-Q.; Wöll, C. Chemical Activity of Oxygen Vacancies on Ceria: a Combined Experimental and Theoretical Study on CeO_2(111). *Phys. Chem. Chem. Phys.* **2014**, *16*, 24165−24168.
(41) Yang, C.; Yu, X.; Heißler, S.; Weidler, P. G.; Nefedov, A.; Wang, Y.; Wöll, C.; Kropp, T.; Paier, J.; Sauer, J. O_2 Activation on Ceria Catalysts—The Importance of Substrate Crystallographic Orientation. *Angew. Chem., Int. Ed.* **2017**, *56*, 16399−16404.
(42) Horn-von Hoegen, M.; Müller, B. H.; Grabosch, T.; Kury, P. Strain Relief during Ge Hut Cluster Formation on Si(001) Studied by High-Resolution LEED and Surface-stress-induced Optical Deflection. *Phys. Rev. B: Condens. Matter Mater. Phys.* **2004**, *70*, 235313.
(43) (a) Horn-von Hoegen, M. Growth of Semiconductor Layers Studied by Spot Profile Analysing Low Energy Electron Diffraction - Part I. *Z. Kristallogr. - Cryst. Mater.* **1999**, *214*, 591−629, Growth of Semiconductor Layers Studied by Spot Profile Analysing Low Energy Electron Diffraction - Part II. 684−721.
(44) Van Hove, M. A.; Weinberg, W. H.; Chan, C.-M. *Low-Energy Electron Diffraction: Experiment, Theory and Surface Structure Determination*; Springer-Verlag: 1986.
(45) Möbus, G.; Saghi, Z.; Sayle, D. C.; Bhatta, U. M.; Stringfellow, A.; Sayle, T. X. T. Dynamics of Polar Surfaces on Ceria Nanoparticles Observed In Situ with Single-Atom Resolution. *Adv. Funct. Mater.* **2011**, *21*, 1971−1976.
(46) Bugnet, M.; Overbury, S. H.; Wu, Z. L.; Epicier, T. Direct Visualization and Control of Atomic Mobility at {100} Surfaces of Ceria in the Environmental Transmission Electron Microscope. *Nano Lett.* **2017**, *17*, 7652−7658.
(47) Binet, C.; Badri, A.; Lavalley, J.-C. Spectroscopic Characterization of the Reduction of Ceria from Electronic Transitions of Intrinsic Point Defects. *J. Phys. Chem.* **1994**, *98*, 6392.